

1 Seasonal variation in aerosol chemistry drives new 2 particle formation and CCN activity in a coastal city, 3 China: insights from year-long online measurements in 4 Fuzhou

5 Zihan Wang¹, Yishu Bian², Fuwang Zhang³, Honglei Wang^{1*}, Wen Lin², Jun Hu⁴,
6 Tianliang Zhao¹, Lijian Shen^{2,5}, Zuxin Xie²

7 ¹ Collaborative Innovation Center on Forecast and Evaluation of Meteorological Disasters (CIC-FEMD),
8 China Meteorological Administration Aerosol-Cloud and Precipitation Key Laboratory, Nanjing
9 University of Information Science and Technology, Nanjing 210044, China

10 ² Fujian Key Laboratory of Severe Weather and Key Laboratory of Straits Severe Weather, China
11 Meteorological Administration, Fuzhou 350001, China

12 ³ Fujian Provincial Environmental Monitoring Central Station, Fuzhou 350003, China

13 ⁴ Fujian Provincial Academy of Environmental Science, Fuzhou 350001, China

14 ⁵ Key Laboratory of Ecosystem Carbon Source and Sink, China Meteorological Administration (ECSS-
15 CMA), Wuxi University, Wuxi 214105, China

16 *Correspondence to:* Honglei Wang (hongleiwang@nuist.edu.cn)

17 **Abstract:** New particle formation (NPF) is an important source of cloud condensation nuclei (CCN),
18 which affects the global climate. Continuous observations in the coastal city of Fuzhou, conducted from
19 June 2021 to May 2022, aimed to study NPF events and their impact on CCN. A total of 46 NPF events
20 were identified, with a frequency of 12.7%. The average formation rate (FR) and growth rate (GR) of
21 particles were $3.94 \pm 8.26 \text{ cm}^{-3} \cdot \text{s}^{-1}$ and $5.20 \pm 1.78 \text{ nm} \cdot \text{h}^{-1}$. The NPF events showed evident seasonal
22 variation: spring (27.17%), fall (9.89%), winter (8.89%), and summer (4.35%). Spring NPF events were
23 characterized by high FR ($5.56 \text{ cm}^{-3} \cdot \text{s}^{-1}$) and suppressed growth processes, while summer, under the
24 dominance of marine winds, exhibited the lowest FR yet the highest GR among all seasons (peak value
25 $11.68 \text{ nm} \cdot \text{h}^{-1}$). The influence of NPF on the chemical composition of $\text{PM}_{2.5}$ and CCN also showed
26 seasonal differences. In summer, NPF generated substantial amounts of sulfate and nitrate, resulting in
27 stronger particle hygroscopicity (>0.6). In fall and winter, higher concentrations of black carbon (BC)
28 and primary organic carbon (POC) led to weaker κ_{inorg} (≤ 0.55). XGBoost-SHAP attribution further
29 quantified that FR is dominated by physical processes (nucleation mode 76.2%, CS 13.8%), with a sharp
30 NH_3 threshold at $4 \mu\text{g} \cdot \text{m}^{-3}$ and a narrow temperature range (20–25 °C). For particle growth, temperature
31 shows a positive linear effect above 20°C, and $\text{RH} > 60\%$ consistently suppresses particle concentrations.

32 The enhancement effect of NPF on CCN was most significant in summer ($E_{N_{CCN}} = 1.64$), accompanied
33 by CCN growth. In spring, the high condensation sink (CS) suppressed growth, leading to an insignificant
34 CCN enhancement effect. In fall and winter, NPF-induced CCN enhancement mainly occurred 3–5 hours
35 after the event, with increases ranging from 13% to 65%, particularly notable at high supersaturation
36 levels (0.8–1.0% SS).

37 **1 Introduction**

38 New particle formation (NPF) is a complex process in which gaseous precursors in the atmosphere
39 nucleate and condense to form new particles, which subsequently grow through condensation,
40 coagulation, and other processes. NPF contributes over 50 % of the global cloud condensation nuclei
41 (CCN), significantly influencing cloud albedo, structure, lifetime, and solar radiation reaching the Earth's
42 surface (Tröstl et al., 2016; Yao et al., 2018). Additionally, efficient nucleation and explosive growth of
43 particles are important sources of haze formation in urban atmospheres, impacting air quality and public
44 health (Kulmala et al., 2021).

45 Although its frequency may vary with season and location, NPF events fundamentally represent
46 competition between aerosol particle sources and sinks. Current research indicates that secondary particle
47 formation is driven by the photochemical oxidation of atmospheric gases. Sulfuric acid and highly
48 oxidized molecules can act as nucleation precursors (Fan et al., 2018; Zaveri et al., 2022). Furthermore,
49 ions may also play a role in particle nucleation, though their significance remains debated (Hirsikko et
50 al., 2011; Kirkby et al., 2016). Pre-existing aerosol particles act as a sink for these precursors, small
51 clusters, and newly formed particles, thereby suppressing NPF occurrence (McMurry and Friedlander,
52 1979). However, frequent NPF events also occur in heavily polluted cities (Sun et al., 2015; Yao et al.,
53 2018). Therefore, the mechanisms governing NPF generation and growth under different atmospheric
54 conditions are still under investigation.

55 NPF events can be described by the formation rate (FR) of nucleation-mode particles and the growth rate
56 (GR) of newly formed particles (Kulmala et al., 2012). The formation rate of 3 nm particles in the
57 boundary layer typically ranges from 0.01 to 10 $\text{cm}^{-3}\text{s}^{-1}$, while the typical growth rate in mid-latitudes
58 ranges from 1 to 20 nm h^{-1} (Kulmala et al., 2004). Yli-Juuti et al. (2011) reported typical growth rates of

59 1.8–10.7 nm·h⁻¹ for 1.5–20 nm particles. Previous studies have shown that NPF is enhanced in the
60 presence of sulfuric acid, alkaline substances, organic acids, and ions (Wang et al., 2011) but suppressed
61 in the presence of nitrogen oxides (NO_x) (Wildt et al., 2014), indicating significant synergistic effects in
62 chemically complex mixtures (Guo et al., 2014). The availability of precursor vapors and the atmospheric
63 chemical environment play decisive roles. H₂SO₄ is a key nucleating species, and its stabilizing
64 co-components, such as ammonia (NH₃) and amines, can dramatically enhance FR (Dunne et al., 2016;
65 Yao et al., 2018; Kirkby et al., 2016). For particle growth, condensation of low-volatility compounds is
66 the dominant process. Sipilä et al. (2010) showed experimentally that early-stage growth is primarily
67 driven by H₂SO₄ condensation.

68 Additionally, NPF occurrence is constrained by atmospheric temperature and humidity (Yu et al., 2017;
69 Yue and Hamill, 1979). Low temperatures promote nucleation, whereas high temperatures suppress it
70 (Sipilä et al., 2010; Dunne et al., 2016; Yu et al., 2017). Dunne et al. (2016) further showed that at low
71 temperatures, the ion-enhancement effect is weak due to suppressed evaporation of neutral clusters, while
72 at ambient temperatures, ions can increase the nucleation rate by about a factor of 15. Consequently,
73 neglecting temperature dependence leads to a marked overestimation of NPF and CCN concentrations in
74 summer (Yu et al., 2017). Hamed et al. (2011), based on observations at multiple continental sites, found
75 that NPF events predominantly occur at relative humidity below 60% and are rare above 80%. The reason
76 is that high relative humidity reduces ultraviolet radiation, lowering the production of OH and H₂SO₄;
77 meanwhile, hygroscopic growth enhances the condensation sink, thereby suppressing new particle
78 formation.

79 Aerosol chemical composition also influences aerosol hygroscopicity, altering its critical diameter and
80 thereby affecting CCN activation and cloud formation (Petters and Kreidenweis, 2007; Williamson et al.,
81 2019; Xu et al., 2020). Petters and Kreidenweis (2007) proposed hygroscopicity parameter (κ) is widely
82 used to quantify the water uptake ability and CCN activity of aerosols. Extensive experimental studies
83 have well characterized the κ values of inorganic salts such as ammonium sulfate, ammonium nitrate,
84 and ammonium bisulfate (Liu et al., 2014; Kuang et al., 2020; Cai et al., 2018; Wu et al., 2016). In the
85 accumulation mode (150–1 μ m), inorganic species contribute about 90 % of the total κ (Liu et al., 2014).

86 Observations across different environments (e.g., mountain, urban) have shown that NPF events typically
87 lead to a significant increase in N_{CCN} (Kuwata et al., 2008; Yue et al., 2011; Fan et al., 2018). Kuwata et
88 al. (2008) observed a clear increase in N_{CCN} at different supersaturation levels after NPF events on Jeju
89 Island, South Korea. Research in Beijing indicated that NPF events could increase local N_{CCN} by 0.4–6
90 times (Yue et al., 2011). In polluted environments, additional condensable species, particularly
91 ammonium nitrate and secondary organic aerosols, can accelerate growth and shorten the time needed
92 for freshly formed particles to reach CCN-active sizes (Zhu et al., 2026). However, some studies suggest
93 that an increase in hydrophobic organic components during subsequent particle growth may inhibit CCN
94 generation. Therefore, understanding the role of different components during particle growth is crucial
95 for assessing their subsequent climate effects.

96 Although NPF research in China is widespread, most studies focus on reporting occurrence frequencies,
97 formation, and growth rates, or are limited to discussing nucleation mechanisms. For instance, NPF event
98 frequencies at sites like Shangdianzi, Mount Tai, and Lin'an in eastern China range from 15% to 29%
99 (Shen et al., 2018). Frequencies in Beijing, Jinan, and Shanghai are approximately 30%, 40%, and 21%,
100 respectively (Jayaratne et al., 2017; Lv et al., 2018; Xiao et al., 2015). Currently, understanding how
101 regional variations in atmospheric oxidants and precursors affect the growth of newly formed particles
102 to CCN sizes, especially the quantification of their CCN efficiency, remains a challenge and frontier in
103 current research (Cai et al., 2018; Kulmala et al., 2021; Rose et al., 2017; Xiao et al., 2015; Yao et al.,
104 2018). Given that Fuzhou is a rapidly developing southeastern coastal city with unique sea-land breeze
105 conditions, a high-temperature and high-humidity environment, and complex pollution emission
106 characteristics, it may have unique NPF mechanisms. However, there is a lack of long-term
107 comprehensive observation or systematically quantified NPF's CCN efficiency in this region. Therefore,
108 this study conducted a one-year comprehensive observation in Fuzhou from June 2021 to May 2022,
109 providing new insights and data support for understanding the CCN efficiency and potential climate
110 relevance of NPF under China's complex atmospheric environment.

111 **2 Data and Methods**

112 **2.1 Observation site**

113 Observation data for this study were collected from June 1, 2021, to May 30, 2022, during comprehensive
114 atmospheric environmental observations conducted at the Fujian Provincial Environmental Monitoring
115 Center Station (26.11°N, 119.30°E, altitude 65 m) and the Fuzhou Meteorological Bureau Station
116 (26.05°N, 119.26°E, altitude 18 m). Both stations are located within Fuzhou's urban area, approximately
117 8 km apart horizontally. The Fujian Provincial Environmental Monitoring Center Station is situated in
118 Gulou District, the central urban area of Fuzhou, surrounded primarily by commercial, residential, and
119 transportation land, representing areas heavily influenced by intense human activities. The Fuzhou
120 Meteorological Bureau Station is located in Cangshan District, southern Fuzhou, approximately 1.5 km
121 east of the Min River. Fuzhou is situated at the Min River estuary and along the East China Sea coast,
122 characterized mainly by plains (average altitude 10–30 m) and a typical East Asian monsoon climate,
123 significantly influenced by sea-land breeze circulation and marine air masses (Hu et al., 2024). Given the
124 short distance (~8 km) and the regional background homogeneity, the local environments of the two sites
125 are not expected to be drastically different, although each is influenced by its specific surroundings (urban
126 vs. riverside). A comparison of air pollutant concentrations between the two sites using nearby national
127 monitoring stations (Table S2).

128 **2.2 Measurement and instrumentation**

129 A CCN counter (CCN-100; DMT, USA) equipped with a continuous flow of 500 cm³/min and a thermal
130 gradient was used to measure CCN concentrations at five SS levels. To maintain counting accuracy, the
131 instrument was regularly calibrated for T gradient, flow rate, pressure, SS, and the optical particle counter
132 (OPC) using standard ammonium sulfate according to the method by Rose et al. (2008). Additionally,
133 zero-point determination was performed before and after each observation to minimize instrumental error.
134 During observations, the measurement interval for each SS level was 10 minutes, and a few minutes were
135 required to stabilize after switching SS levels. Therefore, CCN data collected before reaching stable SS
136 were excluded from subsequent analysis. The typical measurement uncertainty of the CCN-100 is
137 approximately ±10% in Table S1.

138 An online organic carbon/elemental carbon analyzer (Sunset Laboratory semicontinuous OC/EC
139 analyzer, Model-4, Sunset Laboratory Inc., USA) was used to determine organic carbon (OC) and
140 elemental carbon (EC) content in atmospheric particulate matter samples. The instrument provides hourly
141 averaged concentrations. Details of instrument operation can be found in Chang et al. (2017). Based on
142 replicate analyses reported by Zhang et al. (2021), the within-model measurement uncertainties (relative
143 standard deviation) for the Sunset Model-4 are $\pm 3.6\%$ for OC and $\pm 6.8\%$ for EC.

144 A Wide-Range Particle Spectrometer (WPS-1000, MSP) measured aerosol number size distributions (10-
145 350 nm) with a time resolution of 6 minutes across 96 channels. To align with the 1-hour meteorological
146 data, the 6-minute distributions were arithmetically averaged to hourly particle number size distributions.
147 Instrument details and principles are described in Wang et al. (2014). The typical uncertainty for particle
148 size distribution measurements in this size range is approximately $\pm 10\%$ in Table S1.

149 Black carbon (BC) mass concentration was measured using an Aethalometer (AE-33, Magee Scientific)
150 with a time resolution of 1 hour. BC data from the 880 nm wavelength (channel 6) were used (Kirchstetter
151 et al., 2004). The measurement uncertainty is approximately $\pm 10\%$ (Table S1).

152 An online particle chromatograph (MARGA ADI-2080) continuously monitored mass concentrations of
153 soluble aerosol ionic components (SO_4^{2-} , NO_3^- , NH_4^+ , Na^+ , K^+ , Ca^{2+} , Cl^-) and trace gases (NH_3 , HNO_2 ,
154 HNO_3 , HCl , SO_2). Sampling, operation, and internal calibration methods followed Du et al. (2011). The
155 instrument provides hourly averaged concentrations. According to an independent verification study
156 (Battelle, 2009), the measurement precision (median absolute relative percent difference between
157 duplicate units) ranges from 5% for SO_2 to 20% for NH_4^+ , with data completeness $>90\%$ for all major
158 ions.

159 Meteorological data (including wind speed (WS), wind direction (WD), temperature (T), relative
160 humidity (RH), and precipitation) with a time resolution of 1 h were obtained from the Fuzhou Olympic
161 Sports Center Meteorological Station. Data on conventional air pollutants (O_3 , CO , NO_2 , $\text{PM}_{2.5}$, and PM_{10})
162 were sourced from the China National Environmental Monitoring Centre's real-time urban air quality
163 release platform (<https://quotsoft.net/air/>).

164 **2.3 Analysis methods**

165 The growth rate (GR) of new particles was calculated following (Kulmala et al., 2012):

166
$$GR = \frac{\Delta D_m}{\Delta t} \quad (1)$$

167 where D_m is the median diameter of the nucleation mode particles, obtained by fitting a log-normal
 168 distribution to the particle number size distribution. Statistics of the fitting results (see Supplementary
 169 Material) demonstrate that the log-normal distribution represents the observed particle size distributions
 170 well, with the majority of fits yielding high coefficients of determination ($R^2 > 0.85$); only fits with $R^2 > 0.7$
 171 were used to avoid propagating poor-fitting uncertainties. GR describes how rapidly particles grow from
 172 the nucleation size to larger sizes. It is later used to estimate the formation rate of new particles (Eq. 4)
 173 and condensable vapor concentration (Eq. 5) and to evaluate the competition between condensation and
 174 coagulation during NPF events.

175 The condensation sink (CS) reflects the rate at which condensable vapor molecules condense onto the
 176 surface of pre-existing atmospheric particles and was calculated as follows (Kulmala et al., 2012):

177
$$CS = 4\pi D \sum_i \beta_{M,i} \cdot D_i \cdot N_i \quad (2)$$

178 where D is the diffusion coefficient of the vapor (typically assumed to be sulfuric acid), N_i is the number
 179 concentration of particles in a given size bin, and β_M is a correction factor.

180 The coagulation sink (CoagS) reflects the ability and rate of pre-existing atmospheric particles to remove
 181 newly formed nucleation particles via coagulation. For particles of size i , the coagulation sink can be
 182 expressed as:

183
$$CoagS_i = \sum_j K_{ij} N_j \quad (3)$$

184 where N_j is the number concentration of particles in size bin j , and K_{ij} is the Brownian coagulation
 185 coefficient between particles of size j and i .

186 The formation rate (FR) of new particles was calculated following Kulmala et al. (2012):

187
$$FR = \frac{dN_{nuc}}{dt} + CoagS_{nuc} \cdot N_{nuc} + \frac{GR}{\Delta dp} \cdot N_{nuc} + S_{losses} \quad (4)$$

188 where N_{nuc} is the number concentration of nucleation-mode particles. Following the definition by
 189 Kulmala et al. (2012), the nucleation-mode size range in this study was also limited to below 25 nm.
 190 $CoagS_{nuc} \cdot N_{nuc}$ is the flux of particles lost due to coagulation with pre-existing particles, where $CoagS_{nuc}$
 191 is the coagulation sink for nucleation-mode particles. $GR/\Delta dp$ represents the flux of particles growing
 192 out of the nucleation size range (exceeding 25 nm), which is generally negligible under typical

193 atmospheric conditions (Dal Maso et al., 2005). FR is later used to compare NPF event intensity under
194 different meteorological and chemical conditions, and to identify periods with active nucleation. The
195 additional loss term S_{losses} (e.g., dilution due to boundary layer growth, wall losses) was negligible under
196 our field conditions (Dal Maso et al., 2005). For regional NPF events, transport losses can also be ignored.
197 FR is a direct measure of NPF intensity and is later compared across different meteorological and
198 chemical conditions.

199 Condensable vapor concentration (C) and source rate (Q). Assuming that particle growth is dominated
200 by condensation of a low-volatility vapor (typically sulfuric acid), the vapor concentration can be
201 estimated from the observed growth rate (Dal Maso et al., 2005; Kulmala et al., 2012):

$$202 \quad C = A \times \frac{dDp}{dt} \quad (5)$$

203 where Dp is the particle diameter, and A is a constant, which has the value $1.37 \times 10^{-7} \text{ h} \cdot \text{cm}^{-3} \cdot \text{nm}^{-1}$ for a
204 vapor with molecular properties of sulfuric acid (Dal Maso et al., 2005). This provides an upper-limit
205 estimate of the condensable vapor concentration, as it assumes growth is solely due to condensation of
206 the vapor and neglects contributions from coagulation.

207 The CS (Eq. 2) quantifies the rate at which this vapor is removed by pre-existing particles. Under
208 steady-state conditions ($dC/dt=0$), the vapor source rate Q can be derived as (Dal Maso et al., 2005):

$$209 \quad Q = CS \times C \quad (6)$$

210 This source rate represents the net production of condensable vapor needed to maintain the observed
211 growth and is later compared with precursor gas concentrations (e.g., SO_2) to infer the chemical pathways
212 driving NPF.

213 Hygroscopicity parameter (κ_{inorg}) for inorganic species. Due to the lack of organic composition
214 measurements, we estimated the hygroscopicity of the inorganic fraction only. The measured
215 water-soluble ions (SO_4^{2-} , NO_3^- , NH_4^+ , Cl^-) were converted to mass concentrations of inorganic salts
216 using the ion-pairing scheme described in Gysel et al. (2007) and Kuang et al. (2020). The following
217 salts and their κ values (Kuang et al., 2020, Table S2) were considered: $(\text{NH}_4)_2\text{SO}_4$ ($\kappa = 0.48$), NH_4NO_3
218 ($\kappa = 0.58$), NH_4HSO_4 ($\kappa = 0.56$), and NH_4Cl ($\kappa = 0.93$). The volume fraction of each salt was calculated
219 using its density (also from Kuang et al., 2020). The overall inorganic hygroscopicity parameter κ_{inorg}
220 was then obtained by volume-weighted mixing (Petters and Kreidenweis, 2007):

221
$$\kappa_{inorg} = \sum_i \varepsilon_i \kappa_i \quad (7)$$

222 where κ_i and ε_i represent the hygroscopicity parameter and volume fraction of component i in the mixture,
 223 respectively, and i denotes the number of components. This κ_{inorg} represents the hygroscopicity of the
 224 inorganic aerosol components and is used as an upper limit estimate for the total particle hygroscopicity,
 225 as organic matter (typically less hygroscopic) was not included.

226 The concentrations of secondary organic carbon (SOC) and primary organic carbon (POC) were
 227 estimated following (Wu and Yu, 2016):

228
$$POC = (OC/EC)_{min} \times EC \quad (8)$$

229
$$SOC = OC_{total} - (OC/EC)_{pri} \times EC \quad (9)$$

230 where OC_{total} is the measured OC, $(OC/EC)_{min}$ is the minimum (OC/EC) ratio during the observation
 231 period, POC is primary organic carbon, and SOC is secondary organic carbon.

232 The enhancement effect on cloud condensation nuclei number concentration ($E_{N_{CCN}}$) was defined as
 233 the ratio of CCN number concentration after the NPF event to that before the event (Ren et al., 2021):

234
$$E_{N_{CCN}} = N_{CCN, after} / N_{CCN, prior} \quad (10)$$

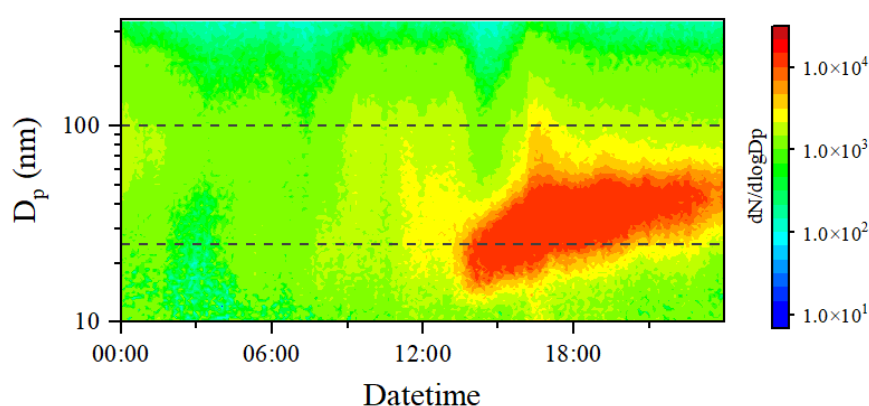
235 where $N_{CCN, after}$ is the average CCN number concentration during the NPF event (from its start to end),
 236 and $N_{CCN, prior}$ is the average CCN concentration during the 2 h before the event. This factor directly links
 237 NPF to potential cloud formation: a value >1 indicates that NPF increases CCN availability.

238 XG Boost-SHAP framework. To quantitatively evaluate the nonlinear effects of meteorological factors
 239 (T, RH) and precursor gases (NH_3 , SO_2) on the particle formation rate (FR), we applied an interpretable
 240 machine learning framework combining XG Boost (Extreme Gradient Boosting) with SHAP (SHapley
 241 Additive exPlanations). A detailed description of the feature selection, model training, validation, and
 242 SHAP interpretation is provided in the supplementary material (Text S1). The main quantitative
 243 thresholds and interaction strengths derived from this analysis are discussed in Section 3.4.

244 **2.4 Identification of NPF events**

245 NPF events were identified based on criteria from Kulmala et al. (2012): (1) significant increase in
 246 nucleation-mode number concentration (N_{nuc}) (diameter 10–25 nm); (2) formation of a new mode lasting
 247 several hours; (3) growth of the newly formed mode over several hours. Additional criteria for NPF

248 identification included: low pre-existing particle number concentration, a clear "banana-shaped"
249 evolution in particle number concentration over time and size, and exclusion of interference from pre-
250 existing particles (especially in urban environments) (Heintzenberg et al., 2007).
251 In this study, a day was defined as an effective NPF day if the nucleation-mode (10–25 nm) particle
252 number concentration increased continuously for at least 2 h from its initial value to its maximum and
253 showed clear growth to larger sizes (e.g., 12–50 nm) over several hours (Fig. 1). Other days were defined
254 as non-NPF days (Leng et al., 2014). During the one-year observation, a total of 46 NPF events and 319
255 non-NPF days were identified.



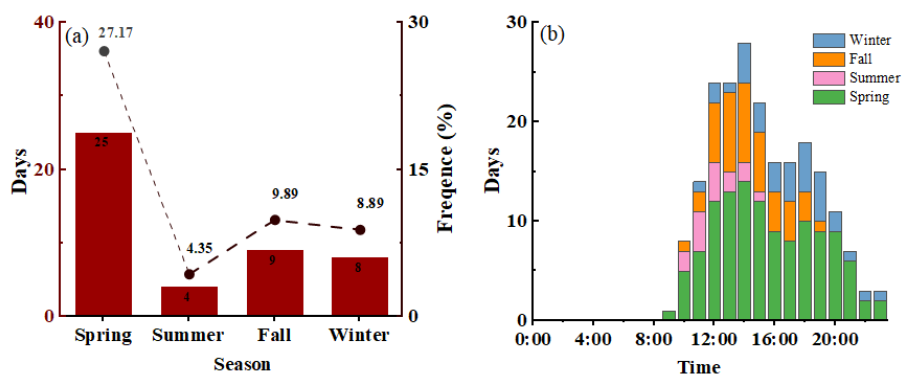
256

257 **Fig. 1** An example NPF event observed on 21 April 2022.

258 **3 Results and Discussion**

259 **3.1 Overall characteristics of NPF occurrence**

260 NPF events in Fuzhou exhibited a distinct seasonal preference. As shown in Fig. 2a, spring was the
261 season with the highest NPF frequency (27.17 %), while summer had the lowest (4.35 %). Fall (9.89 %)
262 and winter (8.89 %) showed intermediate to low frequencies. NPF events mainly occurred between 9:00
263 and 12:00.



264

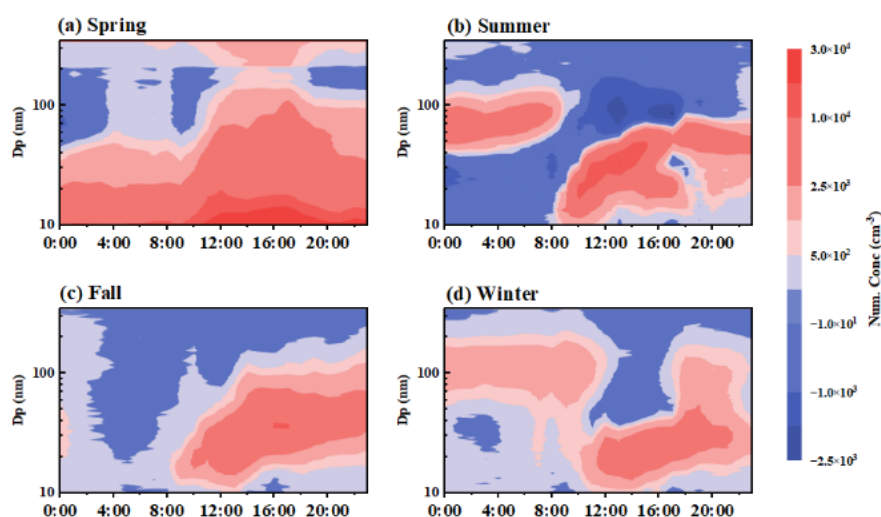
265 **Fig. 2 The occurrence frequency and diurnal distribution of NPF events.**

266 NPF events led to significant increases in nucleation-mode (N_{nuc}) and Aitken-mode (N_{ait}) particle number
 267 concentrations (Fig.S1). Spring showed the highest increase in N_{nuc} (196.7%), while fall showed the
 268 highest increase in N_{ait} (70.5%), indicating differences in new particle formation and subsequent growth
 269 across seasons.

270 NPF days typically corresponded to a lower background of $PM_{2.5}$ and PM_{10} (Fig.S3), indicating that NPF
 271 occurred in relatively clean atmospheres with a weak condensation sink (CS). It should be noted that the
 272 absolute $PM_{2.5}$ and PM_{10} in winter and spring were still relatively high compared to other seasons (Fig.S3),
 273 implying that even on NPF days, these seasons experienced higher pollution levels. In spring, summer,
 274 and winter, POC on NPF days were lower than on non-NPF days, corroborating this point. Meanwhile,
 275 in spring, summer, and fall, SOC was higher on NPF days, suggesting that secondary organic vapors may
 276 actively participate in particle formation and growth.

277 Although spring and winter had heavy background pollution, Fig.S4 shows that the gaseous precursor
 278 SO_2 concentration on NPF days was significantly higher than on non-NPF days (winter: 0.88 vs. 0.76
 279 $\mu g \cdot m^{-3}$; spring: 0.64 vs. 0.53 $\mu g \cdot m^{-3}$). This indicates that in polluted seasons, high gaseous precursors can
 280 overcome the inhibitory effect of a high CS and thus trigger nucleation. In contrast, NPF days in summer
 281 and Fall exhibited a distinctly clean background, with NH_3 and HNO_2 significantly lower than on
 282 non-NPF days (Fig.S4). In summer, fall, and winter, the concentrations of sulfate (SO_4^{2-}), nitrate (NO_3^-),
 283 and ammonium (NH_4^+) on NPF days were significantly lower than on non-NPF days (Fig.S5). This
 284 suggests that in these seasons, the lower pre-existing particles and the reduced CS lessen the consumption
 285 of gaseous precursors, thereby favouring new particle formation and subsequent growth. However, spring
 286 presents a special case in that the SNA (sulfate, nitrate, and ammonium) concentrations on NPF days

287 were comparable to those on non-NPF days (SO_4^{2-} : 4.35 vs. 4.27 $\mu\text{g}\cdot\text{m}^{-3}$). This indicates that spring NPF
 288 events are driven by high precursor concentrations. Even when the background particle level is high, the
 289 abundant supply of gaseous precursors (Fig.S4) can still overcome the inhibition and trigger NPF events.
 290 According to the hygroscopicity parameter (κ_{inorg}) shown in Fig.S6, the κ_{inorg} values on NPF days were
 291 generally lower than on non-NPF days in all seasons except summer, which is generally attributed to an
 292 increased proportion of weakly hygroscopic components in newly formed particles. However, the κ_{inorg}
 293 on NPF days was significantly higher than on non-NPF days in summer. Despite reduced hygroscopicity,
 294 NPF events effectively increased N_{CCN} , which was also combined with higher Cl^- concentration on
 295 summer NPF days in Fig.S5 (0.59 vs. 0.28 $\mu\text{g}\cdot\text{m}^{-3}$). At SS above 0.4%, N_{CCN} on NPF days was higher
 296 than on non-NPF days in all seasons except spring, with the most significant increases observed in winter
 297 and fall (Fig.S7).



298

299 **Fig. 3 The differences in particle number size distributions between NPF days and non-NPF days for each**
 300 **season.**

301 Fig. 3a shows that in spring, particle number concentrations in the 10–20 nm range are generally elevated.
 302 NPF typically occurs from 9:00 to 20:00, with the peak concentration of 10–15 nm particles reaching
 303 29498 cm^{-3} . Concurrently, the concentration of particles >20 nm increases significantly, with some
 304 growing beyond 100 nm. The aerosol size distributions on NPF days in summer, fall, and winter all
 305 exhibit an NPF process pattern similar to that shown in Fig. 1, typically occurring in 09:00–20:00. During
 306 summer NPF events, the maximum particle number concentration reaches approximately 11,410 cm^{-3} ,
 307 with particles growing up to around 50 nm. In fall and winter, peak particle number concentrations are

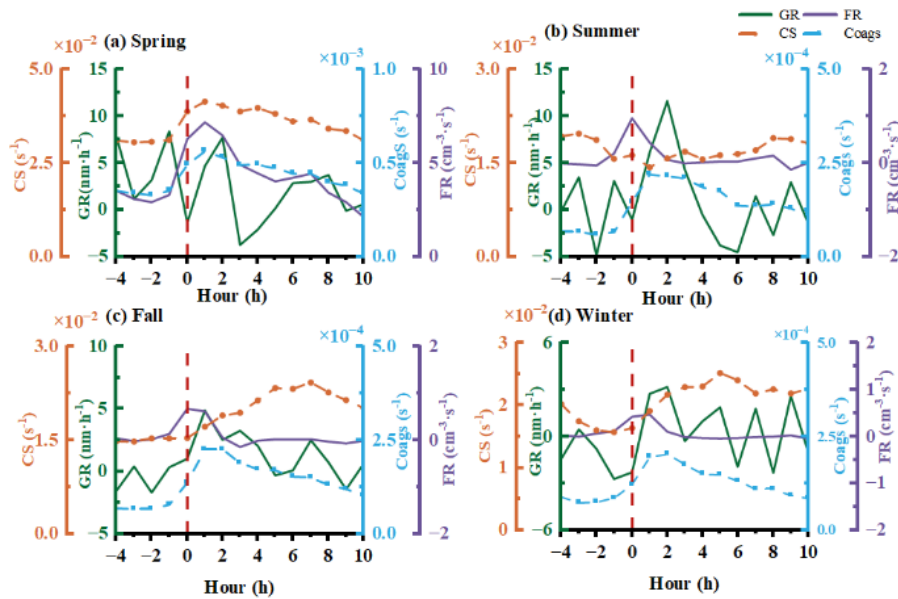
308 lower than in summer (10110 and 5276 cm^{-3}), indicating weaker NPF intensity, and the maximum
 309 particle growth can extend up to 100 nm in these seasons.

310 3.2 Evolution characteristics and key parameters of NPF events

311 Spring NPF events had the highest FR ($7.13 \text{ cm}^{-3} \cdot \text{s}^{-1}$) and the highest CS ($4.1 \times 10^{-2} \text{ s}^{-1}$) among all seasons
 312 (Table 1). Before NPF events (-4 to 0 h), N_{nuc} increased from 5425 to 7701 cm^{-3} , peaking at 1 h (8840
 313 cm^{-3}), then gradually declining. This trend was consistent with changes in the FR (Fig. 4a). FR rose
 314 sharply to $6.31 \text{ cm}^{-3} \cdot \text{s}^{-1}$ at the onset of NPF (0 h) and peaked at $7.21 \text{ cm}^{-3} \cdot \text{s}^{-1}$ at 1 h, demonstrating strong
 315 new particle formation capability. However, intense competition under a high CS background
 316 significantly suppressed subsequent growth. The growth rate (GR) exhibited large fluctuations, reverting
 317 to a negative value at 3 h after an initial peak. N_{ait} increased by only 32% from 0 h to its peak at 2 h,
 318 much lower than in other seasons. Spring NPF events were characterized by strong formation but
 319 suppressed growth under high CS.

320 **Table 1. Seasonal variations in key parameters of NPF events: particle growth rate (GR), formation rate (FR),**
 321 **coagulation sink (CoagS), condensable vapor concentration (C) and its production rate (Q), condensation sink**
 322 **(CS), and hygroscopicity parameter (κ_{inorg}).**

Average	FR ($\text{m}^{-3} \cdot \text{s}^{-1}$)	GR ($\text{nm} \cdot \text{h}^{-1}$)	CS ($\times 10^{-2} \cdot \text{s}^{-1}$)	CoagS ($\times 10^{-4} \text{ s}^{-1}$)	C ($\times 10^7 \text{ cm}^{-3}$)	κ_{inorg}
Total	3.94	5.20	3.1	3.9	16.7	0.56
Spring	7.13	3.69	4.1	5.2	20.1	0.54
Summer	0.40	4.20	1.8	2.0	10.9	0.59
Fall	0.28	2.35	2.0	1.8	9.5	0.55
Winter	0.23	1.87	2.1	1.9	4.7	0.58



323
 324 **Fig. 4 Key NPF parameters: growth rate (GR), formation rate (FR), condensation sink (CS), and coagulation**
 325 **sink (CoagS) for each season. The NPF events in each season have been normalized. The x-axis represents**
 326 **time relative to the NPF event start, where t=0 h is the onset time (defined as the time when the**
 327 **nucleation-mode particle number concentration begins a sustained increase). Negative times indicate hours**
 328 **before the start, and positive times indicate hours after the start. The time axis ranges from –4 h to 10 h,**
 329 **showing the evolution from 4 hours before to 10 hours after the event.**

330 Despite the low average FR ($0.40 \text{ cm}^{-3}\cdot\text{s}^{-1}$, Table 1), summer exhibited the highest average GR (4.20
 331 $\text{nm}\cdot\text{h}^{-1}$), and the lowest average CS ($1.8\times 10^{-2} \text{ s}^{-1}$). In summer NPF events (Fig. 4b), N_{nuc} peaked at 1 h
 332 (3459 cm^{-3}). FR relatively high from 0–2 h ($0.97\text{--}0.44 \text{ cm}^{-3}\cdot\text{s}^{-1}$). The most prominent feature of summer
 333 was the high growth efficiency (GR) under the lowest CS, with a maximum peak of $11.68 \text{ nm}\cdot\text{h}^{-1}$ at 2 h.
 334 After NPF onset in summer, N_{ait} peaked at 3 h (6461.6 cm^{-3}), with the highest increase of 202.91%. This
 335 indicates that the growth process of new particles in summer NPF events was far stronger than particle
 336 formation.

337 Winter had the lowest average FR ($0.23 \text{ cm}^{-3}\cdot\text{s}^{-1}$) and GR ($1.87 \text{ nm}\cdot\text{h}^{-1}$, Table 1). Winter NPF events
 338 were characterized by a low FR and delayed growth under a low condensation sink (CS), as shown in
 339 Table 1. In Fig. 4d, the FR peak observed at 0 h ($0.43 \text{ cm}^{-3}\cdot\text{s}^{-1}$) was the lowest among all seasons,
 340 indicating weak nucleation. In contrast, the growth rate (GR) displayed a distinct multi-peak pattern, with
 341 an initial peak at 2 h ($3.20 \text{ nm}\cdot\text{h}^{-1}$) and subsequent peaks occurring between 5 and 9 h, suggesting that
 342 different mechanisms may have driven particle growth at different stages. Correspondingly, N_{ait} reached
 343 a maximum at 3 h (4794.2 cm^{-3}), which was the lowest seasonal peak (Fig.S8). Nevertheless, N_{ait}

344 remained at relatively high levels ($4500\text{--}4800\text{ cm}^{-3}$) over an extended period from 2 to 6 h, reflecting
345 sustained particle growth throughout the event.

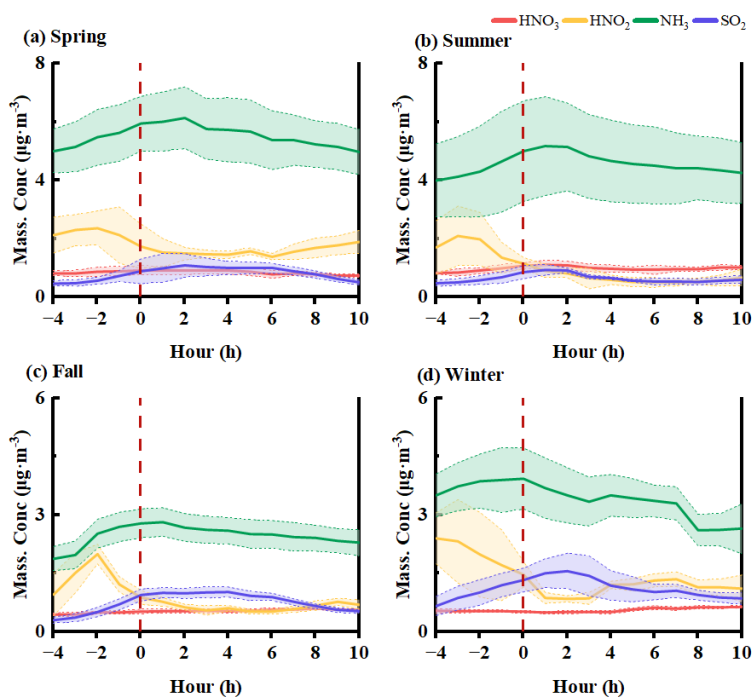
346 Fall presented transitional characteristics, with average FR ($0.28\text{ cm}^{-3}\cdot\text{s}^{-1}$) and GR ($2.35\text{ nm}\cdot\text{h}^{-1}$) higher
347 than winter but lower than spring and summer (Table 1). Fall NPF process parameters showed transitional
348 characteristics between summer and winter, generally similar to winter (Fig. 4c). Its FR peak ($0.68\text{ cm}^{-3}\cdot\text{s}^{-1}$) and GR peak ($4.90\text{ nm}\cdot\text{h}^{-1}$) were higher than winter but much lower than spring and summer. The
349 increase in N_{ait} after NPF onset was 165%, significantly stronger than in winter (Fig.S8). The N_{ait} peak
350 (6240.9 cm^{-3}) occurred latest (4 h) and remained above 5600 cm^{-3} from 5–7 h, higher than winter.
351

352 In summary, spring shows the highest FR ($7.13\text{ cm}^{-3}\cdot\text{s}^{-1}$) but the lowest GR ($3.69\text{ nm}\cdot\text{h}^{-1}$) due to a large
353 CS, indicating strong nucleation yet suppressed growth. Summer achieves the highest GR (peak 11.68
354 $\text{nm}\cdot\text{h}^{-1}$) and the cleanest background (lowest CS), where growth dominates over formation. Fall and
355 winter exhibit low FR and GR with delayed growth, reflecting weaker NPF intensity.

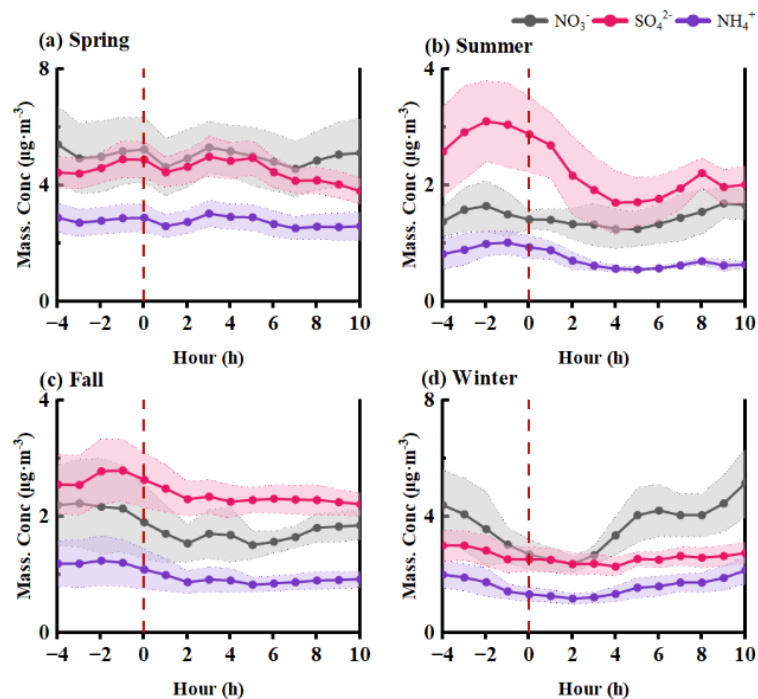
356 **3.3 Influence of chemical composition on NPF events**

357 Spring NPF days were characterized by the highest CS ($4.1\times 10^{-2}\text{ s}^{-1}$) and were predominantly influenced
358 by secondary pollution. Spring NPF events were mainly driven by the continuous transport from the
359 southeast coastal pathway (CL2, 51.33%, Fig.S9a), which supplied high levels of NH_3 ($6.76\pm 2.09\text{ }\mu\text{g}\cdot\text{m}^{-3}$)
360 and HNO_2 ($2.81\pm 2.16\text{ }\mu\text{g}\cdot\text{m}^{-3}$) (Table S4). Consistently, during the NPF events, the frequency of SE/S
361 winds continuously increased and became dominant in the later stage (maximum 38.1%), reflecting the
362 influence of this coastal air mass at the local scale. Before NPF events, gaseous SO_2 and NH_3 increased
363 from 0.47 and $5.01\text{ }\mu\text{g}\cdot\text{m}^{-3}$ to 0.89 and $5.95\text{ }\mu\text{g}\cdot\text{m}^{-3}$, respectively (Fig. 5a). Two hours after NPF onset,
364 their concentrations began to decline continuously, indicating substantial consumption. Mass
365 concentrations of secondary inorganic salts (SO_4^{2-} and NO_3^-) fluctuated between $4.5\text{--}4.8\text{ }\mu\text{g}\cdot\text{m}^{-3}$ and $4\text{--}6$
366 $\mu\text{g}\cdot\text{m}^{-3}$, respectively. Although NO_3^- showed minor fluctuations, it remained at relatively high levels (Fig.
367 6a). NPF events occurred when the temperature was between $18.9\text{--}23.2^\circ\text{C}$ (Fig.S12a), favoring
368 accelerated photochemical reactions and gas-particle conversion of semi-volatile gases (Chen et al.,
369 2023). Wind speeds were generally low ($<1.9\text{ m}\cdot\text{s}^{-1}$), and the atmospheric stratification was stable. After
370 NPF onset, O_3 increased significantly (from 81.1 to $98.8\text{ }\mu\text{g}\cdot\text{m}^{-3}$; Fig.S14a), indicating enhanced
371 atmospheric oxidizability. Precursor gases (SO_2 and NO_2) were oxidized via photochemistry to form

372 NO_3^- and SO_4^{2-} , promoting the generation of secondary inorganic salts and secondary aerosols, including
 373 secondary organic aerosol (Fig.S13a). The high CS background, spring had high-frequency and high-
 374 FR NPF events, primarily attributed to higher precursor gas and strong photochemistry.
 375 However, high CS competed for condensable vapors and scavenged newly formed particles, suppressing
 376 the growth stage of new particles. Additionally, during the NPF event (1–4 h), particle hygroscopicity
 377 decreased from 0.56 at -4 h to 0.53 (Fig.S11).



378
 379 **Fig. 5** The evolution of relevant trace gases (SO_2 , NH_3 , NO_2) for (a) spring, (b) summer, (c) fall, and (d) winter.
 380 The x-axis follows the same normalized time scale as defined in Fig. 4 ($t = 0$ h represents NPF event start).
 381 Shaded bands indicate $\pm 1\sigma$ standard deviation



382

383 **Fig. 6** The evolution of major secondary inorganic ions (SO_4^{2-} , NO_3^- , NH_4^+) for each season. The x-axis follows
 384 the same normalized time scale as defined in Fig. 4 ($t=0$ h represents NPF event start). Shaded bands indicate
 385 $\pm 1\sigma$ standard deviation.

386 CS in summer, fall, and winter were relatively low (around $2.0 \times 10^{-2} \text{ s}^{-1}$), indicating fewer surfaces
 387 available for condensation in the atmosphere.

388 Summer NPF events occurred under a high-temperature environment ($>32^\circ\text{C}$) (Fig.S12b), which inhibits
 389 nucleation (Yu et al., 2017). Two hours after NPF onset (2 h), the frequency of northeasterly (NE) winds
 390 surged from 0% (at -4 h) to 50%, corresponding to marine air mass cluster CL2 (60%), which had a low
 391 average CS of $1.08 \pm 0.31 \times 10^{-2} \text{ s}^{-1}$ (Table S3). The arrival of this air mass diluted local pollutants, causing
 392 PM_{10} to drop from $14.25 \mu\text{g}\cdot\text{m}^{-3}$ at 0 h to $8.75 \mu\text{g}\cdot\text{m}^{-3}$ at 2 h; meanwhile, it supplied abundant gaseous
 393 precursors or enhanced local photochemical activity, leading to continuous increases in SO_2 and NH_3
 394 from 0.48 and $4.00 \mu\text{g}\cdot\text{m}^{-3}$ to peak values of 0.94 and $5.18 \mu\text{g}\cdot\text{m}^{-3}$, respectively, at 2 h (Fig. 5b). Therefore,
 395 despite favorable conditions of low CS and ample sunlight, summer NPF frequency and formation rate
 396 were low. As ozone continued to rise (0–6 h), secondary ions (NO_3^- , SO_4^{2-}) and SOC increased (Fig. 6b
 397 and Fig.S13b). These efficiently condensed onto particle surfaces under a low CS background, achieving
 398 extremely high growth efficiency (GR peak of $11.59 \text{ nm}\cdot\text{h}^{-1}$). κ_{inorg} in the range of 0.61–0.75 was higher
 399 than in other seasons, surging to 0.75 at 3 h after NPF onset. This increase was primarily driven by

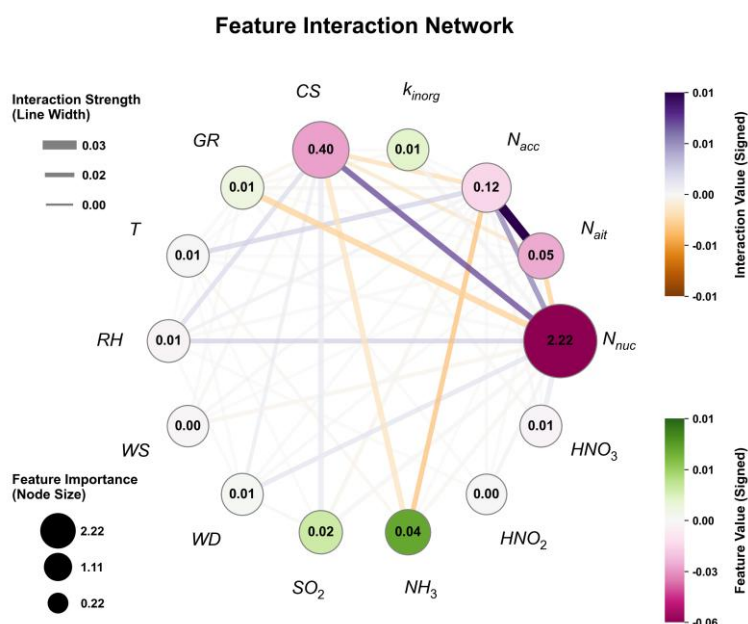
400 prevailing easterly and southerly winds, corresponding to air mass cluster CL3, which had a high κ_{inorg}
401 (0.71). This indicates that inorganic salts of marine origin facilitated the sustained growth of particles.
402 Before Fall NPF events, SO_2 and NH_3 increased from 0.36 and 1.99 $\mu\text{g}\cdot\text{m}^{-3}$ to 2.83 and 2.83 $\mu\text{g}\cdot\text{m}^{-3}$,
403 respectively (Fig. 5c). This stage was dominated by northwesterly winds (NW: 62%) and strongly
404 influenced by continental air masses from CL2 and CL3, which contributed to the initial accumulation
405 of precursor gases (SO_2 and NH_3). The lower temperature (around 22 °C) and high humidity ($\text{RH} > 71\%$)
406 environment (Fig.S12c) favored the combination of sulfuric acid molecules, promoting nucleation
407 (Lehtipalo et al., 2018; Tröstl et al., 2016; Yue and Hamill, 1979). After NPF onset, although atmospheric
408 oxidizability increased continuously (O_3 from 36 to 94 $\mu\text{g}\cdot\text{m}^{-3}$), it was short-lived. Within 1–3 h after
409 NPF onset, the local wind direction shifted notably to southerly (S: 44.4%, Fig.S10c), corresponding on
410 a larger scale to the marine/coastal air mass CL1 (22.22%, Fig.S9c). CL1 served as the most important
411 transport pathway for NH_3 in the fall, with an average concentration as high as 3.13 $\mu\text{g}\cdot\text{m}^{-3}$ (Table S4),
412 substantially higher than that of continental pathways. After 4 h, as O_3 gradually decreased and primary
413 emissions increased, pollutant accumulation occurred, and BC and POC rebounded (Fig.S13c). The
414 contribution of primary emissions (e.g., BC, POC) to aerosols was significantly enhanced, and overall
415 κ_{inorg} (0.55) was low.

416 Winter NPF events were also preceded by an accumulation of gaseous precursors (Fig. 5d). However,
417 elevated emissions from sources such as heating led to high BC and POC during the initial NPF stage
418 (1.86 and 1.02 $\mu\text{g}\cdot\text{m}^{-3}$ at -4 h, Fig.S13d). These abundant primary particles strongly suppressed new
419 particle formation via intense coagulation scavenging, resulting in persistently low formation rates (FR
420 $\leq 0.47 \text{ cm}^{-3}\cdot\text{s}^{-1}$). Photochemical activity was limited under low winter temperatures (Fig.S12d). As
421 temperatures continued to drop later in the event (after 6 h), condensation-driven conversion of gaseous
422 precursors to particles increased (Jokinen et al., 2018). During the 6–10 h period, the high concentrations
423 of precursors reached supersaturation under the low-temperature conditions, promoting the rapid
424 formation of particulate ammonium nitrate (nitrate concentration increased from 4.21 to 5.14 $\mu\text{g}\cdot\text{m}^{-3}$,
425 Fig. 6d). In winter, the air masses were mainly dominated by the northwesterly continental air mass
426 originating from Siberia (CL1, Fig.S9d). Particles within this air mass exhibited relatively high κ_{inorg}
427 (0.59, Table S3), and the introduction of these hygroscopic components effectively offset the dilution of

428 overall hygroscopicity caused by BC and POC. During the 8–10 h period, northwesterly winds persisted,
 429 and their frequency gradually increased, which also explains the gradual increase in κ_{inorg} values (from
 430 0.57 to 0.61, Fig.S11).

431 In summary, in spring, high NH_3 and photochemistry drive strong nucleation, but high CS and secondary
 432 inorganic salts suppress growth. Summer marine air masses provide low CS and high hygroscopicity
 433 ($\kappa_{\text{inorg}} > 0.6$), favoring efficient growth, while fall and winter continental emissions (BC, POC) lower
 434 κ_{inorg} (≤ 0.55) and limit NPF intensity.

435 3.4 Attribution analysis of particle formation and growth



436

437 **Fig. 7 Non-linear response relationships and interaction analysis between core environmental factors and FR.**
 438 **Node size and inner numbers denote feature importance (mean |SHAP|). Node color indicates contribution**
 439 **direction (green: positive; pink: negative). Edge width reflects interaction strength; edge color indicates**
 440 **interaction direction (purple: synergistic; orange: antagonistic).**

441 According to SHAP analysis (Fig.S15), the main contributors to FR in Fuzhou are nucleation mode
 442 (76.2%), CS (13.8%), NH_3 (1.3%), and SO_2 (0.6%). Physical processes explain about 90% of the
 443 variance. A prominent feature is a sharp NH_3 threshold at $4 \mu\text{g}\cdot\text{m}^{-3}$. Below this value, SHAP is
 444 approximately -0.025; above it, SHAP becomes positive and rises to approximately 0.2 at $10 \mu\text{g}\cdot\text{m}^{-3}$. CS
 445 shows a clear inhibition onset at 0.03 s^{-1} , with SHAP dropping from 0 to -0.5 as CS increases to 0.08 s^{-1} .
 446 Temperature has a positive SHAP only within 20–25°C (peak 0.01), decreasing by 40% at 35°C. As

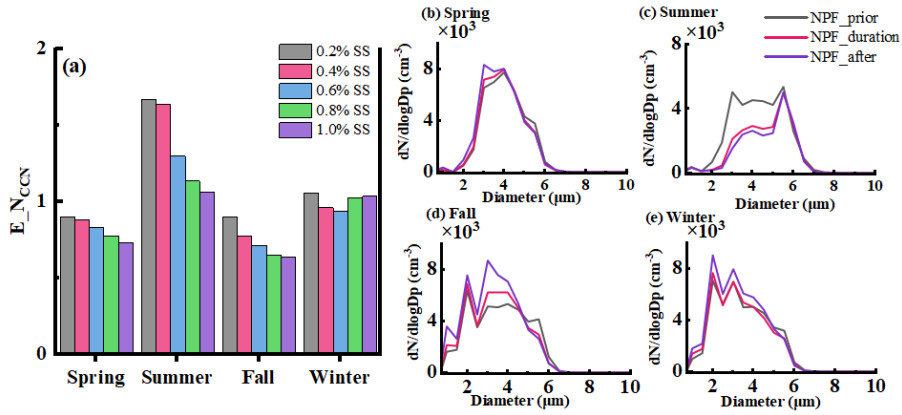
447 shown in Fig. 7, the strongest interaction is between nucleation mode and CS (0.40), far exceeding other
448 pairs (NH₃-nucleation mode: 0.04), highlighting that the net FR is governed by the competition between
449 particle formation and scavenging.

450 For the Aitken mode, the driving forces shift notably. CS remains the top contributor, followed by
451 accumulation mode (13.8%) and nucleation mode (7.1%). As shown in Fig.S16, a key distinction from
452 FR is the temperature response. Instead of a bell shape, SHAP increases linearly from 0 to 0.1 over 20–
453 35°C, indicating that high temperatures accelerate particle growth, enabling a rapid transition from
454 nucleation to the Aitken mode. The NH₃ threshold at 4 µg·m⁻³ persists, showing its continued role in
455 particle growth. RH exerts a linear negative effect, turning SHAP negative above 60%, suggesting
456 hygroscopic growth or coagulation loss. In Fig.S17, the CS-nucleation mode interaction strength is 0.12,
457 lower than in FR but still dominant, implying that strong nucleation can offset high CS losses.

458 In summary, the SHAP attribution reveals two distinct regimes. FR is dominated by CS, accompanied
459 by a sharp chemical trigger (NH₃ > 4 µg·m⁻³) and a narrow temperature window (20–25°C). The Aitken
460 mode, while still influenced by CS, is primarily driven by temperature-accelerated growth (linearly
461 increasing above 20°C). Ammonia acts as a persistent enhancer in both stages, whereas high RH (>60%)
462 consistently suppresses Aitken mode concentrations.

463 **3.5 Particle growth controls CCN formation from NPF events**

464 In summer, although NPF frequency was the lowest, it had a significant enhancing effect on N_{CCN}.
465 E_{N_{CCN}} at 0.4% SS was as high as 1.64 (Fig. 8a). In the initial stage of NPF events (0–2 hours), N_{CCN}
466 showed a sharp decline. At 0.4% SS, it decreased from about 2078 cm⁻³ to 1187 cm⁻³ (Fig.S18b).
467 However, after 2 h, N_{CCN} recovered noticeably and later returned to or even exceeded initial levels. The
468 CCN size distribution (Fig. 8c) showed that during the event, smaller CCN (1–3 µm) decreased, while
469 CCN of 5.5–6.5 µm increased. For instance, CCN at 6 µm increased from 2607.7 to 3147.8 cm⁻³. Summer
470 NPF promoted CCN growth to larger sizes. However, the daily average N_{CCN} on summer NPF days was
471 lower than on non-NPF days, possibly due to the extremely low NPF frequency (4.35 %) and the sharp
472 decline in CCN at the beginning of events, affecting the daily average.



473

474 **Fig.8 The contribution of NPF events to cloud condensation nuclei (CCN) across seasons: (a) CCN**
 475 **enhancement ($E_{N_{CCN}}$), and (b-e) particle number size distributions at 2 hours before, during, and 5 hours**
 476 **after the NPF event for seasons.**

477 Spring NPF events' impact on N_{CCN} showed significant suppression. Throughout the event, N_{CCN} at
 478 various supersaturation levels showed only weak and slow increases. N_{CCN} (0.4% SS, the same as below)
 479 increased from a pre-event average (-4 to -1 h) of about 2636 cm^{-3} to 3192 cm^{-3} at 4 h, then decreased
 480 slowly from 4 to 6 h, with a larger decline at higher supersaturations (Fig.S18a). $E_{N_{CCN}}$ at 0.4% SS was
 481 only 0.88. This phenomenon corresponds to the "high formation, suppressed growth" characteristic of
 482 spring NPF. Despite the explosive generation of nucleation-mode particles, severe competition under
 483 high CS severely hindered subsequent growth of new particles, preventing them from effectively growing
 484 to CCN activation sizes, resulting in a weak or even negative contribution to CCN.

485 In fall events, from 2 h onward, N_{CCN} began to increase, rising from 3471 cm^{-3} to a maximum of 4752
 486 cm^{-3} , forming a high-value plateau lasting from 3 to 8 h (Fig.S18d). After the NPF event, N_{CCN} increased
 487 significantly across the 1–5 μm size range (Fig. 8d). Fall NPF events most effectively and broadly
 488 increased the number of particles available for cloud droplet activation in the atmosphere. Although
 489 $E_{N_{CCN}}$ was lower due to the modest initial stage, the post-event enhancement effect was significant.
 490 This evolution process is consistent with the sustained particle growth process in fall NPF, allowing new
 491 particles to grow steadily to CCN activation sizes.

492 In winter NPF events, N_{CCN} was low in the early stage (0–4 h), with insignificant growth. However, from
 493 5 h onward, N_{CCN} growth became significant, increasing from 4483 cm^{-3} to 6173 cm^{-3} and remaining
 494 stable at high levels (Fig.S18d). During the event, changes in the CCN size distribution were not obvious.

495 However, after the NPF event, CCN in the 2–5 μm size range showed the most significant growth (e.g.,
496 at 2 μm , from 7073.0 to 9045.1 cm^{-3} ; Fig. 8e).

497 **4 Conclusions**

498 This year-long observational study in coastal Fuzhou revealed distinct seasonal patterns in new particle
499 formation (NPF) and its impact on cloud condensation nuclei (CCN). We identified 46 NPF events,
500 which predominantly occurred between 09:00 and 12:00. Key quantitative results include: the highest
501 seasonal formation rate (FR) in spring ($5.56 \text{ cm}^{-3} \text{ s}^{-1}$), the highest growth rate (GR) in summer (peak at
502 11.68 nm h^{-1}), and the strongest CCN enhancement in summer ($E_{\text{NCCN}} = 1.64$ at 0.4 % SS). In fall and
503 winter, CCN increases (13–65 %) lag NPF events by 3–5 h.

504 A total of 46 NPF events occurred during the observation period, with a frequency of 12.7%. NPF event
505 start times were mainly concentrated between 08:00 and 13:00 (accounting for 85 % of all events), with
506 an average duration of 4 h. The annual averages for formation rate (FR), growth rate (GR), condensation
507 sink (CS), coagulation sink (CoagS), and condensable vapor concentration (C) were $3.94 \pm 8.26 \text{ cm}^{-3} \cdot \text{s}^{-1}$,
508 $5.20 \pm 1.78 \text{ nm} \cdot \text{h}^{-1}$, $4.2 \times 10^{-2} \text{ s}^{-1}$, $5.6 \times 10^{-4} \text{ s}^{-1}$, and $16.7 \times 10^7 \text{ cm}^{-3}$, respectively.

509 The seasonal contrast is mechanistically driven by the interplay between precursor availability, CS, and
510 aerosol chemistry. Spring conditions favor high FR due to strong photochemistry and abundant
511 precursors, but high CS suppresses subsequent growth. In summer, the occurrence of NPF events is often
512 accompanied by a transition in sea-land breeze circulation. The northerly land breeze shifts to
513 northeasterly/easterly sea breezes, effectively transporting clean marine air masses to the observation site.
514 This reduces the CS to its seasonal minimum ($1.08 \pm 0.31 \times 10^{-2} \text{ s}^{-1}$), favoring efficient particle growth and
515 thereby sustaining the highest growth rate (GR) observed across all seasons. The chemical composition
516 shifts from being dominated by sulfate and sea salt with high hygroscopicity in summer ($\kappa_{\text{inorg}} > 0.6$) to
517 low hygroscopicity in fall ($\kappa_{\text{inorg}} = 0.55$), directly modulating particle hygroscopicity and cloud
518 condensation nuclei (CCN) activation potential.

519 Using XGBoost-SHAP, FR is dominated by nucleation mode (76.2 %) and CS (13.8 %). $\text{NH}_3 > 4 \mu\text{g} \cdot \text{m}^{-3}$
520 enhances FR, $\text{CS} > 0.03 \text{ s}^{-1}$ inhibits FR (SHAP drops to -0.5 at 0.08 s^{-1}), and Temperature benefits FR
521 only within 20–25 °C. For Aitken mode, temperature linearly promotes growth above 20°C, while

522 RH > 60 % suppresses it. The strong nucleation-CS interaction (0.40) highlights the competition between
523 formation and scavenging.

524 This work demonstrates that the climatic impact of NPF in coastal urban areas is not simply a function
525 of its occurrence frequency or formation strength. Instead, it is seasonally modulated by a competition
526 between formation and growth-sink processes, and by the resulting aerosol chemical composition. The
527 decoupling of high FR from effective CCN production (as in spring) implies that climate models using
528 NPF frequency as a proxy for aerosol indirect effects may overestimate the impact in high-CS coastal
529 regions. Conversely, the efficient growth and CCN enhancement in summer suggest that even infrequent
530 NPF events can substantially influence cloud properties in such environments. These insights are crucial
531 for developing more accurate parameterizations of aerosol-cloud-climate interactions in rapidly
532 developing coastal zones.

533 **Data availability**

534 Data will be made available on request.

535 **Author contributions**

536 Conceptualization was completed by ZW and HW. Formal analysis and software modification were
537 carried out by ZW and HW. The initial draft was written by ZW, incorporating tables provided by HW.
538 The first draft was revised by ZW, HW, and YB, with input from HW, YB, FZ, WL, JH, LS, and ZX;
539 subsequent versions of the manuscript were reviewed and edited by all authors. Data curation and
540 collection were conducted by all authors. Funding acquisition was secured by HW.

541 **Competing interests**

542 The authors declare that they have no conflict of interest.

543 **Disclaimer**

544 Copernicus Publications remains neutral with regard to jurisdictional claims made in the text, published
545 maps, institutional affiliations, or any other geographical representation in this paper. While Copernicus

546 Publications makes every effort to include appropriate place names, the final responsibility lies with the
547 authors. Views expressed in the text are those of the authors and do not necessarily reflect the views of
548 the publisher.

549 **Acknowledgements**

550 The authors are grateful for the assistance with sample collection. We would like to thank the China
551 National Environmental Monitoring Centre's real-time urban air quality release platform
552 (<http://106.37.208.233:20035/>)

553 **Financial support**

554 This study was supported by the National Key Research and Development Program of China (Grant No.,
555 2022YFC3701204), the National Natural Science Foundation of China (42505181 and U22A20578),
556 Natural Science Foundation of Fujian Province, China (2024J01168 and 2023R1014003), the Natural
557 Science Foundation of Jiangsu Province (BK20231300), and the Open Fund of Fujian Key Laboratory
558 of Severe Weather and Key Laboratory of Straits Severe Weather (2024KFKT05).

559 **References**

560 Battelle: Environmental Technology Verification Report: Applikon MARGA Semi-Continuous Ambient
561 Air Monitoring System, U.S. Environmental Protection Agency, available at:
562 <https://nepis.epa.gov/Exe/ZyPURL.cgi?Dockey=P100FZOD.pdf> (last access: 24 April 2026), 2009.

563 Cai, M., Tan, H., Chan, C. K., Qin, Y., Xu, H., Li, F., Schurman, M. I., Liu, L., and Zhao, J.: The size-
564 resolved cloud condensation nuclei (CCN) activity and its prediction based on aerosol hygroscopicity
565 and composition in the pearl delta river (PRD) region during wintertime 2014, *Atmos. Chem. Phys.*, 18,
566 16419–16437, <https://doi.org/10.5194/acp-18-16419-2018>, 2018.

567 Chang, Y., Deng, C., Cao, F., Cao, C., Zou, Z., Liu, S., Lee, X., Li, J., Zhang, G., and Zhang, Y.:
568 Assessment of carbonaceous aerosols in Shanghai, China—Part 1: long-term evolution, seasonal
569 variations, and meteorological effects, *Atmos. Chem. Phys.*, 17, 9945–9964, [https://doi.org/10.5194/acp-](https://doi.org/10.5194/acp-17-9945-2017)
570 17-9945-2017, 2017.

571 Chen, M., Titcombe, M., Jiang, J., Jen, C., Kuang, C., Fischer, M. L., Eisele, F. L., Siepmann, J. I.,
572 Hanson, D. R., Zhao, J., and McMurry, P. H.: Acid–base chemical reaction model for nucleation rates in
573 the polluted atmospheric boundary layer, *Proc. Natl. Acad. Sci.*, 109, 18713–18718,
574 <https://doi.org/10.1073/pnas.1210285109>, 2012.

575 Dal Maso, M. D., Kulmala, M., Riipinen, I., Wagner, R., Hussein, T., Aalto, P., and Lehtinen, K.:
576 Formation and growth of fresh atmospheric aerosols: eight years of aerosol size distribution data from
577 SMEAR II, hyytiälä, Finland, *Boreal Environ. Res.*, 10, 323–336, 2005.

578 Du, H., Kong, L., Cheng, T., Chen, J., Yang, X., Zhang, R., Han, Z., Yan, Z., and Ma, Y.: Insights into
579 ammonium particle-to-gas conversion: non-sulfate ammonium coupling with nitrate and chloride,
580 *Aerosol Air Qual. Res.*, 10, 589–595, <https://doi.org/10.4209/aaqr.2010.04.0034>, 2010.

581 Dunne, E. M., Gordon, H., Kürten, A., Almeida, J., Duplissy, J., Williamson, C., Ortega, I. K., Pringle,
582 K. J., Adamov, A., Baltensperger, U., Barmet, P., Benduhn, F., Bianchi, F., Breitenlechner, M., Clarke,
583 A., Curtius, J., Dommen, J., Donahue, N. M., Ehrhart, S., Flagan, R. C., Franchin, A., Guida, R., Hakala,
584 J., Hansel, A., Heinritzi, M., Jokinen, T., Kangasluoma, J., Kirkby, J., Kulmala, M., Kupc, A., Lawler,
585 M. J., Lehtipalo, K., Makhmutov, V., Mann, G., Mathot, S., Merikanto, J., Miettinen, P., Nenes, A.,
586 Onnela, A., Rap, A., Reddington, C. L. S., Riccobono, F., Richards, N. A. D., Rissanen, M. P., Rondo,
587 L., Sarnela, N., Schobesberger, S., Sengupta, K., Simon, M., Sipilä, M., Smith, J. N., Stozkhov, Y., Tomé,
588 A., Tröstl, J., Wagner, P. E., Wimmer, D., Winkler, P. M., Worsnop, D. R., and Carslaw, K. S.: Global
589 atmospheric particle formation from CERN CLOUD measurements, *Science*, 354, 1119–1124,
590 <https://doi.org/10.1126/science.aaf2649>, 2016.

591 Chen, Y., Wang, X., Dai, W., Wang, Q., Guo, X., Liu, Y., Qi, W., Shen, M., Zhang, Y., Li, L., Cao, Y.,
592 Wang, Y., and Li, J.: Particle Number Size Distribution of Wintertime Alpine Aerosols and Their
593 Activation as Cloud Condensation Nuclei in the Guanzhong Plain, Northwest China, *J. Geophys. Res.:*
594 *Atmos.*, 128, e2022JD037877, <https://doi.org/10.1029/2022JD037877>, 2023.

595 Fan, J., Rosenfeld, D., Zhang, Y., Giangrande, S. E., Li, Z., Machado, L. A. T., Martin, S. T., Yang, Y.,
596 Wang, J., Artaxo, P., Barbosa, H. M. J., Braga, R. C., Comstock, J. M., Feng, Z., Gao, W., Gomes, H.
597 B., Mei, F., Pöhlker, C., Pöhlker, M. L., Pöschl, U., and de Souza, R. A. F.: Substantial convection and

598 precipitation enhancements by ultrafine aerosol particles, *Science*, 359, 411–418,
599 <https://doi.org/10.1126/science.aan8461>, 2018.

600 Guo, S., Hu, M., Zamora, M. L., Peng, J., Shang, D., Zheng, J., Du, Z., Wu, Z., Shao, M., Zeng, L.,
601 Molina, M. J., and Zhang, R.: Elucidating severe urban haze formation in China, *Proc. Natl. Acad. Sci.*,
602 111, 17373–17378, <https://doi.org/10.1073/pnas.1419604111>, 2014.

603 Heintzenberg, J., Wehner, B., and Birmili, W.: ‘How to find bananas in the atmospheric aerosol’: new
604 approach for analyzing atmospheric nucleation and growth events, *Tellus B*, 59, 273–282,
605 <https://doi.org/10.1111/j.1600-0889.2007.00249.x>, 2007.

606 Gysel, M., Crosier, J., Topping, D. O., Whitehead, J. D., Bower, K. N., Cubison, M. J., Williams, P. I.,
607 Flynn, M. J., McFiggans, G. B., and Coe, H.: Closure study between chemical composition and
608 hygroscopic growth of aerosol particles during TORCH2, *Atmos. Chem. Phys.*, 7, 6131–6144,
609 <https://doi.org/10.5194/acp-7-6131-2007>, 2007.

610 Hamed, A., Korhonen, H., Sihto, S.-L., Joutsensaari, J., Järvinen, H., Petäjä, T., Arnold, F., Nieminen,
611 T., Kulmala, M., Smith, J. N., Lehtinen, K. E. J., and Laaksonen, A.: The role of relative humidity in
612 continental new particle formation, *J. Geophys. Res.: Atmos.*, 116, D03206,
613 <https://doi.org/10.1029/2010JD014186>, 2011.

614 Hirsikko, A., Nieminen, T., Gagné, S., Lehtipalo, K., Manninen, H. E., Ehn, M., Hörrak, U., Kerminen,
615 V.-M., Laakso, L., McMurry, P. H., Mirme, A., Mirme, S., Petäjä, T., Tammet, H., Vakkari, V., Vana,
616 M., and Kulmala, M.: Atmospheric ions and nucleation: a review of observations, *Atmos. Chem. Phys.*,
617 11, 767–798, <https://doi.org/10.5194/acp-11-767-2011>, 2011.

618 Hu, J., Shi, C., Ni, E., Liu, J., Zhai, S., Zhao, T., Jiang, B., Jiang, D., Wang, H., and Huang, Q.:
619 Recirculated transport mechanism aggravates ozone pollution over the mountainous coastal region:
620 Increased contribution from vertical mixing, *Atmos. Environ.*, 332, 120617,
621 <https://doi.org/10.1016/j.atmosenv.2024.120617>, 2024.

622 Jayaratne, R., Pushpawela, B., He, C., Li, H., Gao, J., Chai, F., and Morawska, L.: Observations of
623 particles at their formation sizes in beijing, china, *Atmos. Chem. Phys.*, 17, 8825–8835,
624 <https://doi.org/10.5194/acp-17-8825-2017>, 2017.

625 Jokinen, T., Sipilä, M., Kontkanen, J., Vakkari, V., Tisler, P., Duplissy, E.-M., Junninen, H.,
626 Kangasluoma, J., Manninen, H. E., Petäjä, T., Kulmala, M., Worsnop, D. R., Kirkby, J., Virkkula, A.,
627 and Kerminen, V.-M.: Ion-induced sulfuric acid–ammonia nucleation drives particle formation in coastal
628 antarctica, *Sci. Adv.*, <https://doi.org/10.1126/sciadv.aat9744>, 2018.

629 Kawana, K., Miyazaki, Y., Omori, Y., Tanimoto, H., Kagami, S., Suzuki, K., Yamashita, Y., Nishioka,
630 J., Deng, Y., Yai, H., and Mochida, M.: Number-Size Distribution and CCN Activity of Atmospheric
631 Aerosols in the Western North Pacific During Spring Pre-Bloom Period: Influences of Terrestrial and
632 Marine Sources, *J. Geophys. Res.: Atmos.*, 127, e2022JD036690, <https://doi.org/10.1029/2022JD036690>,
633 2022.

634 Kirchstetter, T. W., Novakov, T., and Hobbs, P. V.: Evidence that the spectral dependence of light
635 absorption by aerosols is affected by organic carbon, *J. Geophys. Res.: Atmos.*, 109, 2004JD004999,
636 <https://doi.org/10.1029/2004JD004999>, 2004.

637 Kirkby, J., Duplissy, J., Sengupta, K., Frege, C., Gordon, H., Williamson, C., Heinritzi, M., Simon, M.,
638 Yan, C., Almeida, J., Tröstl, J., Nieminen, T., Ortega, I. K., Wagner, R., Adamov, A., Amorim, A.,
639 Bernhammer, A.-K., Bianchi, F., Breitenlechner, M., Brilke, S., Chen, X., Craven, J., Dias, A., Ehrhart,
640 S., Flagan, R. C., Franchin, A., Fuchs, C., Guida, R., Hakala, J., Hoyle, C. R., Jokinen, T., Junninen, H.,
641 Kangasluoma, J., Kim, J., Krapf, M., Kürten, A., Laaksonen, A., Lehtipalo, K., Makhmutov, V., Mathot,
642 S., Molteni, U., Onnela, A., Peräkylä, O., Piel, F., Petäjä, T., Praplan, A. P., Pringle, K., Rap, A., Richards,
643 N. A. D., Riipinen, I., Rissanen, M. P., Rondo, L., Sarnela, N., Schobesberger, S., Scott, C. E., Seinfeld,
644 J. H., Sipilä, M., Steiner, G., Stozhkov, Y., Stratmann, F., Tomé, A., Virtanen, A., Vogel, A. L., Wagner,
645 A. C., Wagner, P. E., Weingartner, E., Wimmer, D., Winkler, P. M., Ye, P., Zhang, X., Hansel, A.,
646 Dommen, J., Donahue, N. M., Worsnop, D. R., Baltensperger, U., Kulmala, M., Carslaw, K. S., and
647 Curtius, J.: Ion-induced nucleation of pure biogenic particles, *Nature*, 533, 521–526,
648 <https://doi.org/10.1038/nature17953>, 2016.

649 Kuang, Y., He, Y., Xu, W., Zhao, P., Cheng, Y., Zhao, G., Tao, J., Ma, N., Su, H., Zhang, Y., Sun, J.,
650 Cheng, P., Yang, W., Zhang, S., Wu, C., Sun, Y., and Zhao, C.: Distinct diurnal variation in organic
651 aerosol hygroscopicity and its relationship with oxygenated organic aerosol, *Atmos. Chem. Phys.*, 20,
652 865–880, <https://doi.org/10.5194/acp-20-865-2020>, 2020.

653 Kulmala, M., Vehkamäki, H., Petäjä, T., Dal Maso, M., Lauri, A., Kerminen, V.-M., Birmili, W., and
654 McMurry, P. H.: Formation and growth rates of ultrafine atmospheric particles: a review of observations,
655 *J. Aerosol Sci.*, 35, 143–176, <https://doi.org/10.1016/j.jaerosci.2003.10.003>, 2004.

656 Kulmala, M., Petäjä, T., Nieminen, T., Sipilä, M., Manninen, H. E., Lehtipalo, K., Dal Maso, M., Aalto,
657 P. P., Junninen, H., Paasonen, P., Riipinen, I., Lehtinen, K. E. J., Laaksonen, A., and Kerminen, V.-M.:
658 Measurement of the nucleation of atmospheric aerosol particles, *Nat. Protoc.*, 7, 1651–1667,
659 <https://doi.org/10.1038/nprot.2012.091>, 2012.

660 Kulmala, M., Dada, L., Daellenbach, K. R., Yan, C., Stolzenburg, D., Kontkanen, J., Ezhova, E., Hakala,
661 S., Tuovinen, S., Kokkonen, T. V., Kurppa, M., Cai, R., Zhou, Y., Yin, R., Baalbaki, R., Chan, T., Chu,
662 B., Deng, C., Fu, Y., Ge, M., He, H., Heikkinen, L., Junninen, H., Liu, Y., Lu, Y., Nie, W., Rusanen, A.,
663 Vakkari, V., Wang, Y., Yang, G., Yao, L., Zheng, J., Kujansuu, J., Kangasluoma, J., Petäjä, T., Paasonen,
664 P., Järvi, L., Worsnop, D., Ding, A., Liu, Y., Wang, L., Jiang, J., Bianchi, F., and Kerminen, V.-M.: Is
665 reducing new particle formation a plausible solution to mitigate particulate air pollution in beijing and
666 other chinese megacities?, *Faraday Discuss.*, 226, 334–347, <https://doi.org/10.1039/D0FD00078G>, 2021.

667 Kuwata, M., Kondo, Y., Miyazaki, Y., Komazaki, Y., Kim, J. H., Yum, S. S., Tanimoto, H., and
668 Matsueda, H.: Cloud condensation nuclei activity at Jeju Island, Korea in spring 2005, *Atmos. Chem.*
669 *Phys.*, 8, 2933–2948, <https://doi.org/10.5194/acp-8-2933-2008>, 2008.

670 Lehtipalo, K., Yan, C., Dada, L., Bianchi, F., Xiao, M., Wagner, R., Stolzenburg, D., Ahonen, L. R.,
671 Amorim, A., Baccarini, A., Bauer, P. S., Baumgartner, B., Bergen, A., Bernhammer, A.-K.,
672 Breitenlechner, M., Brilke, S., Buchholz, A., Mazon, S. B., Chen, D., Chen, X., Dias, A., Dommen, J.,
673 Draper, D. C., Duplissy, J., Ehn, M., Finkenzeller, H., Fischer, L., Frege, C., Fuchs, C., Garmash, O.,
674 Gordon, H., Hakala, J., He, X., Heikkinen, L., Heinritzi, M., Helm, J. C., Hofbauer, V., Hoyle, C. R.,
675 Jokinen, T., Kangasluoma, J., Kerminen, V.-M., Kim, C., Kirkby, J., Kontkanen, J., Kürten, A., Lawler,
676 M. J., Mai, H., Mathot, S., MauldinIII, R. L., Molteni, U., Nichman, L., Nie, W., Nieminen, T., Ojdanic,
677 A., Onnela, A., Passananti, M., Petäjä, T., Piel, F., Pospisilova, V., Quéléver, L. L. J., Rissanen, M. P.,
678 Rose, C., Sarnela, N., Schallhart, S., Schuchmann, S., Sengupta, K., Simon, M., Sipilä, M., Tauber, C.,
679 Tomé, A., Tröstl, J., Väisänen, O., Vogel, A. L., Volkamer, R., Wagner, A. C., Wang, M., Weitz, L.,
680 Wimmer, D., Ye, P., Ylisirniö, A., Zha, Q., Carslaw, K. S., Curtius, J., Donahue, N. M., Flagan, R. C.,

681 Hansel, A., Riipinen, I., Virtanen, A., Winkler, P. M., Baltensperger, U., Kulmala, M., and Worsnop, D.
682 R.: Multicomponent new particle formation from sulfuric acid, ammonia, and biogenic vapors, *Sci. Adv.*,
683 <https://doi.org/10.1126/sciadv.aau5363>, 2018.

684 Leng, C., Zhang, Q., Tao, J., Zhang, H., Zhang, D., Xu, C., Li, X., Kong, L., Cheng, T., Zhang, R., Yang,
685 X., Chen, J., Qiao, L., Lou, S., Wang, H., and Chen, C.: Impacts of new particle formation on aerosol
686 cloud condensation nuclei (CCN) activity in shanghai: case study, *Atmos. Chem. Phys.*, 14, 11353–
687 11365, <https://doi.org/10.5194/acp-14-11353-2014>, 2014.

688 Liu, H. J., Zhao, C. S., Nekat, B., Ma, N., Wiedensohler, A., van Pinxteren, D., Spindler, G., Müller, K.,
689 and Herrmann, H.: Aerosol hygroscopicity derived from size-segregated chemical composition and its
690 parameterization in the north China plain, *Atmos. Chem. Phys.*, 14, 2525–2539,
691 <https://doi.org/10.5194/acp-14-2525-2014>, 2014.

692 Liu, P. F., Zhao, C. S., Göbel, T., Hallbauer, E., Nowak, A., Ran, L., Xu, W. Y., Deng, Z. Z., Ma, N.,
693 Mildenerger, K., Henning, S., Stratmann, F., and Wiedensohler, A.: Hygroscopic properties of aerosol
694 particles at high relative humidity and their diurnal variations in the North China Plain, *Atmos. Chem.*
695 *Phys.*, 11, 3479–3494, <https://doi.org/10.5194/acp-11-3479-2011>, 2011.

696 Lv, G., Sui, X., Chen, J., Jayaratne, R., and Mellouki, A.: Investigation of new particle formation at the
697 summit of Mt. Tai, China, *Atmos. Chem. Phys.*, 18, 2243–2258, [https://doi.org/10.5194/acp-18-2243-](https://doi.org/10.5194/acp-18-2243-2018)
698 2018, 2018.

699 McMurry, P. H. and Friedlander, S. K.: New particle formation in the presence of an aerosol, *Atmos.*
700 *Environ.* (1967), 13, 1635–1651, [https://doi.org/10.1016/0004-6981\(79\)90322-6](https://doi.org/10.1016/0004-6981(79)90322-6), 1979.

701 Petters, M. D. and Kreidenweis, S. M.: A single parameter representation of hygroscopic growth and
702 cloud condensation nucleus activity, *Atmos. Chem. Phys.*, 7, 1961–1971, [https://doi.org/10.5194/acp-7-](https://doi.org/10.5194/acp-7-1961-2007)
703 1961-2007, 2007.

704 Ren, J., Chen, L., Fan, T., Liu, J., Jiang, S., and Zhang, F.: The NPF Effect on CCN Number
705 Concentrations: A Review and Re-Evaluation of Observations From 35 Sites Worldwide, *Geophys. Res.*
706 *Let.*, 48, e2021GL095190, <https://doi.org/10.1029/2021GL095190>, 2021.

707 Rose, C., Sellegri, K., Moreno, I., Velarde, F., Ramonet, M., Weinhold, K., Krejci, R., Andrade, M.,
708 Wiedensohler, A., Ginot, P., and Laj, P.: CCN production by new particle formation in the free
709 troposphere, *Atmos. Chem. Phys.*, 17, 1529–1541, <https://doi.org/10.5194/acp-17-1529-2017>, 2017.

710 Rose, D., Gunthe, S. S., Mikhailov, E., Frank, G. P., Dusek, U., Andreae, M. O., and Pöschl, U.:
711 Calibration and measurement uncertainties of a continuous-flow cloud condensation nuclei counter
712 (DMT-CCNC): CCN activation of ammonium sulfate and sodium chloride aerosol particles in theory
713 and experiment, *Atmos. Chem. Phys.*, 8, 1153–1179, <https://doi.org/10.5194/acp-8-1153-2008>, 2008.

714 Shen, X., Sun, J., Kivekäs, N., Kristensson, A., Zhang, X., Zhang, Y., Zhang, L., Fan, R., Qi, X., Ma, Q.,
715 and Zhou, H.: Spatial distribution and occurrence probability of regional new particle formation events
716 in eastern China, *Atmos. Chem. Phys.*, 18, 587 – 599, <https://doi.org/10.5194/acp-18-587-2018>, 2018.

717 Sipilä, M., Berndt, T., Petäjä, T., Brus, D., Vanhanen, J., Stratmann, F., Patokoski, J., Mauldin, R. L.,
718 Hyvärinen, A.-P., Lihavainen, H., and Kulmala, M.: The role of sulfuric acid in atmospheric nucleation,
719 *Science*, 327, 1243–1246, <https://doi.org/10.1126/science.1180315>, 2010.

720 Sun, Y. L., Wang, Z. F., Du, W., Zhang, Q., Wang, Q. Q., Fu, P. Q., Pan, X. L., Li, J., Jayne, J., and
721 Worsnop, D. R.: Long-term real-time measurements of aerosol particle composition in beijing, china:
722 seasonal variations, meteorological effects, and source analysis, *Atmos. Chem. Phys.*, 15, 10149–10165,
723 <https://doi.org/10.5194/acp-15-10149-2015>, 2015.

724 Tröstl, J., Chuang, W. K., Gordon, H., Heinritzi, M., Yan, C., Molteni, U., Ahlm, L., Frege, C., Bianchi,
725 F., Wagner, R., Simon, M., Lehtipalo, K., Williamson, C., Craven, J. S., Duplissy, J., Adamov, A.,
726 Almeida, J., Bernhammer, A.-K., Breitenlechner, M., Brilke, S., Dias, A., Ehrhart, S., Flagan, R. C.,
727 Franchin, A., Fuchs, C., Guida, R., Gysel, M., Hansel, A., Hoyle, C. R., Jokinen, T., Junninen, H.,
728 Kangasluoma, J., Keskinen, H., Kim, J., Krapf, M., Kürten, A., Laaksonen, A., Lawler, M., Leiminger,
729 M., Mathot, S., Möhler, O., Nieminen, T., Onnela, A., Petäjä, T., Piel, F. M., Miettinen, P., Rissanen, M.
730 P., Rondo, L., Sarnela, N., Schobesberger, S., Sengupta, K., Sipilä, M., Smith, J. N., Steiner, G., Tomè,
731 A., Virtanen, A., Wagner, A. C., Weingartner, E., Wimmer, D., Winkler, P. M., Ye, P., Carslaw, K. S.,
732 Curtius, J., Dommen, J., Kirkby, J., Kulmala, M., Riipinen, I., Worsnop, D. R., Donahue, N. M., and
733 Baltensperger, U.: The role of low-volatility organic compounds in initial particle growth in the
734 atmosphere, *Nature*, 533, 527–531, <https://doi.org/10.1038/nature18271>, 2016.

735 Wang, H., Zhu, B., Shen, L., An, J., Yin, Y., and Kang, H.: Number size distribution of aerosols at Mt.
736 Huang and nanjing in the Yangtze River delta, china: effects of air masses and characteristics of new
737 particle formation, *Atmos. Res.*, 150, 42–56, <https://doi.org/10.1016/j.atmosres.2014.07.020>, 2014.

738 Wang, Z. B., Hu, M., Yue, D. L., Zheng, J., Zhang, R. Y., Wiedensohler, A., Wu, Z. J., Nieminen, T.,
739 and Boy, M.: Evaluation on the role of sulfuric acid in the mechanisms of new particle formation for
740 beijing case, *Atmos. Chem. Phys.*, 11, 12663–12671, <https://doi.org/10.5194/acp-11-12663-2011>, 2011.

741 Wildt, J., Mentel, T. F., Kiendler-Scharr, A., Hoffmann, T., Andres, S., Ehn, M., Kleist, E., M \ddot{u} sgen, P.,
742 Rohrer, F., Rudich, Y., Springer, M., Tillmann, R., and Wahner, A.: Suppression of new particle
743 formation from monoterpene oxidation by NO $_x$, *Atmos. Chem. Phys.*, 14, 2789–2804,
744 <https://doi.org/10.5194/acp-14-2789-2014>, 2014.

745 Williamson, C. J., Kupc, A., Axisa, D., Bilsback, K. R., Bui, T., Campuzano-Jost, P., Dollner, M., Froyd,
746 K. D., Hodshire, A. L., Jimenez, J. L., Kodros, J. K., Luo, G., Murphy, D. M., Nault, B. A., Ray, E. A.,
747 Weinzierl, B., Wilson, J. C., Yu, F., Yu, P., Pierce, J. R., and Brock, C. A.: A large source of cloud
748 condensation nuclei from new particle formation in the tropics, *Nature*, 574, 399–403,
749 <https://doi.org/10.1038/s41586-019-1638-9>, 2019.

750 Wu, C. and Yu, J. Z.: Determination of primary combustion source organic carbon-to-elemental carbon
751 (OC / EC) ratio using ambient OC and EC measurements: secondary OC-EC correlation minimization
752 method, *Atmos. Chem. Phys.*, 16, 5453–5465, <https://doi.org/10.5194/acp-16-5453-2016>, 2016.

753 Wu, Z. J., Zheng, J., Shang, D. J., Du, Z. F., Wu, Y. S., Zeng, L. M., Wiedensohler, A., and Hu, M.:
754 Particle hygroscopicity and its link to chemical composition in the urban atmosphere of Beijing, china,
755 during summertime, *Atmos. Chem. Phys.*, 16, 1123–1138, <https://doi.org/10.5194/acp-16-1123-2016>,
756 2016.

757 Xiao, S., Wang, M. Y., Yao, L., Kulmala, M., Zhou, B., Yang, X., Chen, J. M., Wang, D. F., Fu, Q. Y.,
758 Worsnop, D. R., and Wang, L.: Strong atmospheric new particle formation in winter in urban shanghai,
759 china, *Atmos. Chem. Phys.*, 15, 1769–1781, <https://doi.org/10.5194/acp-15-1769-2015>, 2015.

760 Xu, W., Ovadnevaite, J., Fossum, K. N., Lin, C., Huang, R.-J., O’Dowd, C., and Ceburnis, D.: Aerosol
761 hygroscopicity and its link to chemical composition in the coastal atmosphere of Mace Head: marine and

762 continental air masses, *Atmos. Chem. Phys.*, 20, 3777–3791, <https://doi.org/10.5194/acp-20-3777-2020>,
763 2020.

764 Yao, L., Garmash, O., Bianchi, F., Zheng, J., Yan, C., Kontkanen, J., Junninen, H., Mazon, S. B., Ehn,
765 M., Paasonen, P., Sipilä, M., Wang, M., Wang, X., Xiao, S., Chen, H., Lu, Y., Zhang, B., Wang, D., Fu,
766 Q., Geng, F., Li, L., Wang, H., Qiao, L., Yang, X., Chen, J., Kerminen, V.-M., Petäjä, T., Worsnop, D.
767 R., Kulmala, M., and Wang, L.: Atmospheric new particle formation from sulfuric acid and amines in a
768 chinese megacity, *Science*, <https://doi.org/10.1126/science.aao4839>, 2018.

769 Yli-Juuti, T., Nieminen, T., Hirsikko, A., Aalto, P. P., Asmi, E., Hörrak, U., Manninen, H. E., Patokoski,
770 J., Dal Maso, M., Petäjä, T., Rinne, J., Kulmala, M., and Riipinen, I.: Growth rates of nucleation mode
771 particles in hyytiälä during 2003&minus- 2009: variation with particle size, season, data analysis method
772 and ambient conditions, *Atmos. Chem. Phys.*, 11, 12865–12886, [https://doi.org/10.5194/acp-11-12865-](https://doi.org/10.5194/acp-11-12865-2011)
773 2011, 2011.

774 Yu, F., Luo, G., Nadykto, A. B., and Herb, J.: Impact of temperature dependence on the possible
775 contribution of organics to new particle formation in the atmosphere, *Atmos. Chem. Phys.*, 17, 4997–
776 5005, <https://doi.org/10.5194/acp-17-4997-2017>, 2017.

777 Yue, D. L., Hu, M., Zhang, R. Y., Wu, Z. J., Su, H., Wang, Z. B., Peng, J. F., He, L. Y., Huang, X. F.,
778 Gong, Y. G., and Wiedensohler, A.: Potential contribution of new particle formation to cloud
779 condensation nuclei in Beijing, *Atmos. Environ.*, 45, 6070–6077,
780 <https://doi.org/10.1016/j.atmosenv.2011.07.037>, 2011.

781 Yue, G. K. and Hamill, P.: The homogeneous nucleation rates of H₂SO₄-H₂O aerosol particles in air, *J.*
782 *Aerosol Sci.*, 10, 609–614, [https://doi.org/10.1016/0021-8502\(79\)90023-5](https://doi.org/10.1016/0021-8502(79)90023-5), 1979.

783 Zaveri, R. A., Wang, J., Fan, J., Zhang, Y., Shilling, J. E., Zelenyuk, A., Mei, F., Newsom, R., Pekour,
784 M., Tomlinson, J., Comstock, J. M., Shrivastava, M., Fortner, E., Machado, L. A. T., Artaxo, P., and
785 Martin, S. T.: Rapid growth of anthropogenic organic nanoparticles greatly alters cloud life cycle in the
786 Amazon rainforest, *Science Advances*, 8, eabj0329, <https://doi.org/10.1126/sciadv.abj0329>, 2022.

787 Zhan, Y., Xie, M., Gao, D., Wang, T., Zhang, M., and An, F.: Characterization and source analysis of
788 water-soluble inorganic ionic species in PM_{2.5} during a wintertime particle pollution episode in Nanjing,
789 china, *Atmos. Res.*, 262, 105769, <https://doi.org/10.1016/j.atmosres.2021.105769>, 2021.

790 Zhu, W., Shang, S., Wang, J., Wu, Y., Deng, Z., Ran, L., Kuang, Y., Tang, G., Huang, X., Pan, X., Liu,
791 L., Xu, W., Sun, Y., Hu, B., Wang, Z., and Liu, Z.: Oxidation-driven acceleration of NPF-to-CCN
792 conversion under polluted atmosphere: evidence from mountain-top observations in Yangtze River delta,
793 *Atmos. Chem. Phys.*, 26, 1947–1965, <https://doi.org/10.5194/acp-26-1947-2026>, 2026